JACS
JOURNAL OF THE AMERICAN CHEMICAL SOCIETY
Article
pubs.acs.org/JACS

Evidence for Anisotropic Electronic Coupling of Charge Transfer States in Weakly Interacting Organic Semiconductor Mixtures

Valentina Belova,[*,†] Paul Beyer,[‡] Eduard Meister,[§] Theresa Linderl,[§] Marc-Uwe Halbich,[∥] Marina Gerhard,[∥] Stefan Schmidt,[§] Thomas Zechel,[§] Tino Meisel,[‡] Alexander V. Generalov,[⊥] Ana Sofia Anselmo,[#] Reinhard Scholz,[††] Oleg Konovalov,[‡‡] Alexander Gerlach,[†] Martin Koch,[∥] Alexander Hinderhofer,[†] Andreas Opitz,[*,‡] Wolfgang Brütting,[*,§] and Frank Schreiber[*,†]

[†]Institut für Angewandte Physik, Universität Tübingen, Tübingen 72076, Germany
[‡]Department of Physics, Humboldt-Universität zu Berlin, Berlin 10099, Germany
[§]Institute of Physics, Experimental Physics IV, University of Augsburg, Augsburg 86135, Germany
[∥]Faculty of Physics and Material Sciences Center, Philipps-Universität Marburg, Marburg 35037, Germany
[⊥]Max IV Laboratory, Lund University, Lund SE-221 00, Sweden
[#]Helmholtz-Zentrum Berlin für Materialien und Energie GmbH, Berlin 14109, Germany
[††]Dresden Integrated Center for Applied Physics and Photonic Materials (IAPP), Technische Universität Dresden, Dresden 01062, Germany
[‡‡]European Synchrotron Radiation Facility, Grenoble 38000, France

Supporting Information

ABSTRACT: We present a comprehensive investigation of the charge-transfer (CT) effect in weakly interacting organic semiconductor mixtures. The donor−acceptor pair diindenoperylene (DIP) and *N*,*N*′-bis(2-ethylhexyl)-1,7-dicyanoperylene-3,4/9,10-bis(dicarboxyimide) (PDIR−CN_2) has been chosen as a model system. A wide range of experimental methods was used in order to characterize the structural, optical, electronic, and device properties of the intermolecular interactions. By detailed analysis, we demonstrate that the partial CT in this weakly interacting mixture does not have a strong effect on the ground state and does not generate a hybrid orbital. We also find a strong CT transition in light absorption as well as in photo- and electroluminescence. By using different layer sequences and compositions, we are able to distinguish electronic coupling in-plane vs out-of-plane and, thus, characterize the anisotropy of the CT state. Finally, we discuss the impact of CT exciton generation on charge-carrier transport and on the efficiency of photovoltaic devices.

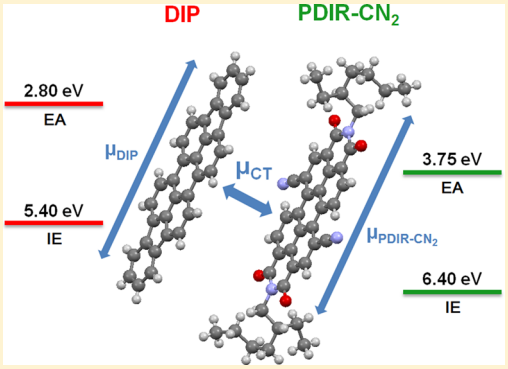

INTRODUCTION

One of the fundamental processes in devices based on organic semiconductors (OSC) is the charge transfer (CT) between electron donor (D) and electron acceptor (A) molecules at interfaces or in molecular mixed systems.[1−4] The concept of CT as a mechanism of intermolecular interaction was described in the framework of Mulliken theory in the 1950s.[5] In this theory, a donor and an acceptor form a CT complex, where the energy levels of the ground and excited states depend on the overlap of the D/A wave functions, and an electronic transition to the excited state is accompanied by partial or integer charge transfer.

In a simplified view, we can distinguish three nominal cases of CT systems depending on the degree of intermolecular interaction (Figure 1). To the first category (Figure 1a), we may assign systems where the intermolecular energy gap ΔE_{DA} between the highest-occupied molecular orbital (HOMO) of a donor and the lowest-unoccupied molecular orbital (LUMO) of an acceptor are almost identical to the individual energy gaps of the donor ΔE_D or the acceptor ΔE_A. Thus, CT in the electronic ground state (GS-CT) is unlikely to be observed, and integer charges are mainly transferred because of exciton (D* and A* states) formation and dissociation. As examples, the material combinations employed for planar heterojunction (PHJ) solar cells such as α-sexithiophene (6T)/diindenoperylene (DIP),[6] 6T/tetra-phenyldibenzoperiflanthene (DBP),[7] and DBP/zinc chlorodipyrrin (ZCl)[8] can be considered. A second category (Figure 1b) describes weakly coupled molecules, where $\Delta E_{DA} < \Delta E_D$ or ΔE_A. These weakly bound

Received: February 15, 2017
Published: June 1, 2017

ACS Publications © 2017 American Chemical Society

DOI: 10.1021/jacs.7b01622
J. Am. Chem. Soc. 2017, 139, 8474−8486

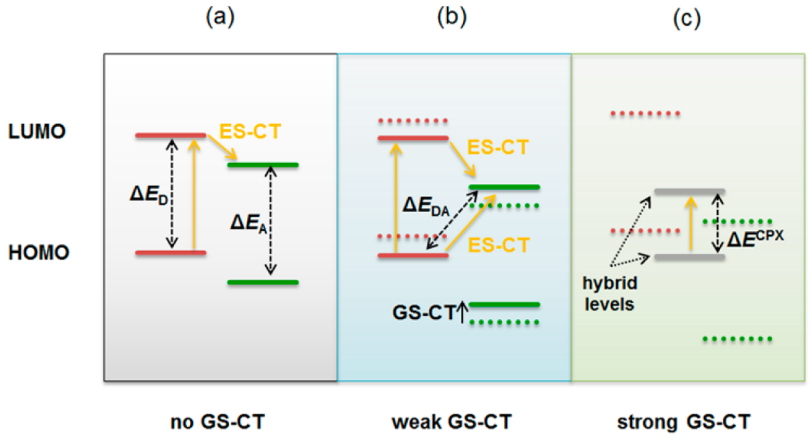

Figure 1. Simplified schematic illustration of possible scenarios for energy levels at interfaces. (a) $\Delta E_{DA} \approx \Delta E_D$ or ΔE_A, No ground-state interaction present, charges are transferred through molecular excitons formed preliminarily (D* or A*), yellow arrows depict electron transitions; (b) $\Delta E_{DA} < \Delta E_D$ or ΔE_A, Weakly coupled molecules, partial GS-CT contributes to energy level shift, original levels are dotted, CT can occur either under direct excitation or via exciton dissociation; (c) $\Delta E_{DA} \ll \Delta E_D$ or ΔE_A, Strong ground-state interaction, orbital hybridization resulting in energy splitting of a CT complex (ΔE^{CPX}) is observed. Note that the full picture may be more complex and that for electronic transitions, the exciton-binding energy must be taken into account.[10]

complexes result, on average, in a partial charge transfer from the donor to the acceptor in the ground state, and the CT state can be directly excited, but the molecular orbitals do not undergo a significant change. Examples for such mixed molecular systems are DIP/fullerene (C_{60}),[9] DBP/C_{60},[7] DIP/*N*,*N*′-dioctyl-3,4,9,10-perylene tetracarboxylicdiimide (PTCDI−C_8),[11] and *N*,*N*′-bis(1-naphthyl)-*N*,*N*′-diphenyl-1,1′-biphenyl-4,4′-diamine (NPD)/C_{60}.[12] In a third category (Figure 1c), we have systems with stronger intermolecular coupling, where ΔE_{DA} is insignificant compared to the energy gap of each component, ΔE_D or ΔE_A. In this case, the formation of hybridized molecular orbitals with an energy splitting ΔE^{CPX} can be observed, as has been shown for quaterthiophene (4T)/2,3,5,6-tetrafluoro-7,7,8,8-tetracyanoquinodimethane (F_4−TCNQ),[13] pentacene (PEN)/F_4−TCNQ[14] or picene (PIC)/F_4−TCNQ.[15]

We note that the three different scenarios presented in Figure 1 change gradually from one to another and sharp boundaries are difficult to define. As an additional criterion for classification, one may consider the strength of the direct absorption into a CT state. For example, a very weak CT absorption may be observed for type (a), requiring highly sensitive techniques, whereas type (b) reveals relatively strong CT bands detectable with standard ultraviolet−visible-near-infrared (UV/vis/NIR) absorption spectroscopy. So far, photoinduced CT via exciton formation and dissociation (as in (a)) and CT doping (as in (c)) are widely discussed in the literature. However, here we focus on the type (b) (weak ground-state interaction−strong excited-state interaction) and discuss fundamental characteristics as a complete understanding of the CT mechanism in this type of systems has not been achieved yet.

In the present paper, we comprehensively study the CT mechanism in organic binary mixtures starting from morphological and structural investigations, via complementary forms of spectroscopy, to the implications in device applications. As a case study, we chose thin films of the small-molecule semiconductors diindenoperylene (DIP) and *N*,*N*′-bis(2-ethylhexyl)-1,7-dicyanoperylene-3,4/9,10-bis(dicarboxyimide) (PDIR−CN_2, where R = C_8H_{17}, branched[16]) (Figure 2a,b). Both materials belong to the group of perylene derivatives

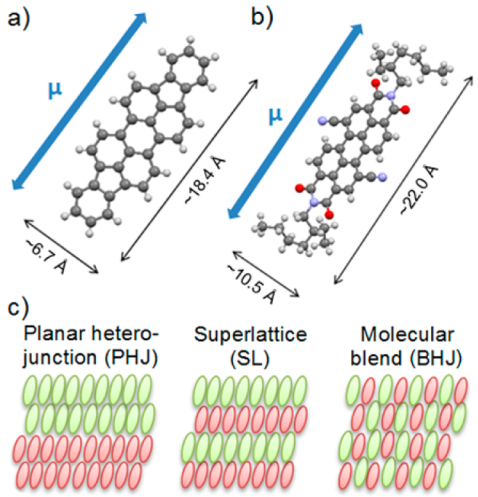

Figure 2. Chemical structure of DIP (part (a), C atoms−dark gray, H atoms−light gray) and PDIR−CN_2 (part (b), O − red, N − blue);[16] The blue arrow indicates the orientation of the transition dipole moment μ (optical axis) of the lowest electronic transition; (c) Sketch of the structural geometries (red ellipsoids−donor, green ellipsoids−acceptor).

widely used as electron donors and acceptors in organic electronic devices.[17−19] They are structurally well-defined and therefore can serve as a model system.

We chose three different architectures (Figure 2c). A planar heterojunction (PHJ) was chosen as the simplest model, and we chose a two-component mixed bulk-heterojunction film (BHJ) with different mixing ratios and a superlattice (SL) consisting of 20 alternating monolayers as an intermediate case. DIP and PDIR−CN_2 have a similar backbone size (Figure 2a,b) that enable good intermixing upon coevaporation and, as a consequence, more interface area.

We organize our results as follows: In the "Structural Characterization" section, we discuss morphological and structural properties studied by means of atomic force microscopy (AFM) and X-ray scattering. We provide evidence for the formation of a CT complex between DIP and PDIR−CN_2 in the ground state using Fourier transform infrared

DOI: 10.1021/jacs.7b01622
J. Am. Chem. Soc. 2017, 139, 8474−8486

spectroscopy (FTIR) and ultraviolet photoelectron spectroscopy (UPS) and in the excited state using optical absorption and emission spectroscopies as described in the corresponding sections. In the section "Device Behavior" we demonstrate the impact of CT states on charge separation and transport in photovoltaic devices. Finally, we summarize our findings and discuss them with respect to the classification given above.

EXPERIMENTAL SECTION

The samples were prepared by organic molecular-beam deposition (OMBD) in vacuum.[20,21] For structural and optical investigations, two types of substrates were used: silicon wafers with a native oxide layer (thickness $d_{ox} \approx 2$ nm) and glass. During film growth, the substrates were kept at 297 K, and base pressure in the chamber did not exceed 10^{-9} mbar. Mixed films were produced by coevaporation of DIP (Prof. J. Pflaum, Universität Würzburg, Germany) and PDIR−CN_2 (ActivInk N1400 Polyera, U.S.A.) in different mixing ratios. The nominal thickness and deposition rate were monitored with a water-cooled quartz crystal microbalance (QCM) during film growth: 20 and 100 nm for each coevaporated and pristine film, 20 nm for each layer in a PHJ, and 1.7 nm for each monolayer of a SL (10 pairs of D/A layers) with a total rate of 0.5 nm/min.

For the preparation of the solar cells and the samples for UPS and conductivity measurements, we used glass substrates coated with prestructured 140 nm indium−tin oxide (ITO). A polymeric hole injection layer of HIL 1.3 (Clevios Heraeus) was spin-coated from an aqueous solution on the ITO, followed by annealing at 125 °C. DIP and PDIR−CN_2 were evaporated onto the substrate by OMBD under a vacuum of 10^{-7} mbar with rates of 3−6 nm/min and 0.2−6 nm/min, respectively, depending on the mixing ratio or sample structure. Aluminum (100 nm) was used as the cathode material, and it was deposited thermally through a shadow mask onto a previously applied 5 nm-thick exciton blocking layer of bathocuproine (BCP). For these measurements, we have modified the BHJ configuration by sandwiching the mixed layer between two thin neat layers of DIP and PDIR−CN_2, respectively. This configuration will be denoted planar-mixed heterojunction (PMHJ).

The surface morphology was measured by AFM using a JPK Nanowizard II instrument in tapping mode under ambient conditions. Image analysis was performed with Gwyddion.[22] X-ray diffraction measurements were performed at the beamline ID10 of the European Synchrotron Radiation Facility (Grenoble, France) and at the beamline X04SA of the Swiss Lightsource (Villigen, Switzerland) using a focused beam with a wavelength of λ = 0.9398 Å and λ = 0.8857 Å, respectively. The raw data were processed and corrected for footprint and background contributions. XRR data fitting was done with GenX[23] by evaluation of the Kiessig fringes with the Parratt formalism.[24] IR spectra were obtained in transmission mode with a Vertex 70 (Bruker) FTIR spectrometer at the Brewster's angle of silicon (74°). The theoretical IR spectra were calculated with TURBOMOLE. UV−vis−NIR absorption spectra were obtained using a Varian Cary 5000 spectrophotometer (Agilent Technologies) at normal incidence. Photoluminescence spectra were acquired using a Horiba Jobin Yvon Labram HR 800 spectrometer with a CCD-1024 × 256-OPEN-3S9 detector. Excitation for PL was performed using a frequency-doubled Nd:YAG laser at a wavelength of 532 nm and a He:Ne laser at 633 nm; excitation was conducted at temperatures of 297 and 90 K. The anisotropic components of the extinction coefficient were determined by variable-angle spectroscopic ellipsometry (VASE) using a Woollam M-2000 ellipsometer with a rotating compensator.[25]

The photoemission experiments were performed at the beamlines PM4 (end station LowDosePES) and UE52 (end station UE52-PGM Multicolor) at the synchrotron storage ring BESSY II at Helmholtz-Zentrum Berlin. The time-resolved PL studies were carried out with a Hamamatsu streak camera. The excitation wavelength was set to 460 nm, employing a lithium triborate crystal for second harmonic generation.

Conductivity measurements were performed on blended films with different mixing ratios deposited on glass substrates using interdigitated ITO electrodes in the dark and under illumination with a halogen lamp using a Keithley 2612A source-meter unit.

Current density vs voltage (j-V) characteristics of solar cells were recorded with a Keithley 236 source-measure unit. The currents were measured in the dark and under one sun simulated AM1.5G, 100 mW/cm^2 illumination with a Xe-lamp. Electroluminescence measurements were carried out by using a CCD camera (PyLoN:100BR eXcelon, Princeton Instruments) coupled with a spectrometer (SP2300i, Princeton Instruments). The measurements were performed under a dc voltage driven by a Keithley 2400 source meter. Incident-photon-to-current efficiency (IPCE) spectra were detected under monochromatic illumination (Omni - λ300 Monochromator/Spectrograph, Zolix Instruments Co., Ltd.).

Details on near-edge X-ray absorption fine structure (NEXAFS) spectroscopy measurements (performed at MAX IV) are given in the Supporting Information.

RESULTS AND DISCUSSION

Structural Characterization. Prior to the examination of CT, the two compounds were characterized regarding the structural organization of the molecules during simultaneous or consecutive growth, as this is crucial for the formation of D/A interfaces. For this purpose, AFM and X-ray scattering measurements were applied.

AFM images of the thin films are shown in Figure 3 (for height profiles see SI). The morphology of the pristine DIP film reveals a typical "wedding-cake-like" structure[26] with a step size 1.6−1.8 nm corresponding to one monolayer of upright-standing DIP molecules and a root-mean-square (σ_{RMS}) surface roughness of 2.85 nm. For all mixed films, as well as pristine PDIR−CN_2 films, the grain sizes decrease significantly. This results in very smooth surfaces and σ_{RMS} roughnesses below 1 nm, with no clear molecular steps to distinguish. Therefore, based on these AFM results, we have no evidence of phase separation.

The surface of the SL consists of similarly small grains with a roughness comparable to the molecular blends. The PHJ surface has a roughness similar to pristine DIP. The top layer of PDIR−CN_2 adopts a grain size of about 115 nm, which is comparable to the average DIP grain size underneath.

For more detailed structural information, we applied X-ray scattering techniques (i.e. reflectivity (XRR) and grazing-incidence X-ray diffraction (GIXD)). Specular scans are shown in Figure 4. The first Bragg peak of pristine DIP (red curve) is observed at q_z = 0.37 Å^{-1}, which corresponds to the standing-up or σ-orientation of DIP with an out-of-plane lattice spacing of $d_{(001)} \approx 16.9$ Å[26,27] and an ∼83° inclination angle of the molecular plane relative to the surface plane. One Bragg peak and a weak second-order reflection are observed in the XRR scan of the pristine PDIR−CN_2, for which the branched alkyl side chains inhibit long-range crystal formation.[16] As known from the literature, PDIR−CN_2 forms a unit cell with an inclination angle of ∼53°, which gives an out-of-plane lattice spacing of $d_{(001)}$ = 16.5 Å.[16] The q_z value of the Bragg peak from the XRR scan (lowermost curve) corresponds to $d_{(001)}$ = 17.1 Å, which almost coincides with pristine DIP. In the case of the blended systems, the second-order Bragg reflection still persists in films with excess DIP (3:1) but disappears with increasing PDIR−CN_2 fraction. The exact peak maxima of the coevaporated films cannot be properly quantified through a strong interference effect.[28] Nevertheless, an apparent gradual shift toward lower q_z points to changes in the lattice parameter.

DOI: 10.1021/jacs.7b01622
J. Am. Chem. Soc. 2017, 139, 8474−8486

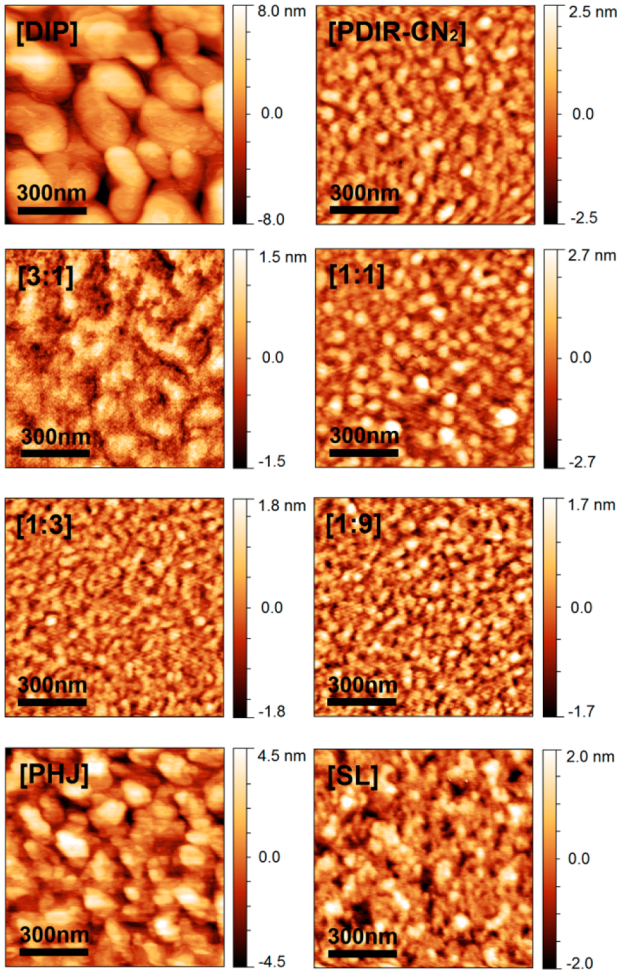

Figure 3. AFM images for pristine films, coevaporated blends, and heterostructures (the top layers of PHJ and SL consist of PDIR−CN_2 molecules). For surface profiles see SI.

We used a three layer model (bulk Si-substrate−SiO_2 layer−organic film) to determine the film thickness d and roughness σ of the mixtures from the XRR (Table S1). Regarding planar heterostructures, PDIR−CN_2 molecules grown on top of a DIP layer adopt the same standing-up configuration (Figure 4, uppermost curve) and form a layer with increased roughness because of the rough DIP layer underneath. Roughness of the SL according to XRR is quite low, which may serve as evidence for the layer-by-layer growth mode or preferential filling of gaps.[28]

The results of GIXD experiments on pristine and coevaporated films are shown in Figure 5. Very strong in-plane reflections of pristine DIP are less intense and broader in nonequimolar mixtures with an excess of pristine DIP molecules. In the equimolar mixture, DIP reflections almost vanish, which demonstrates a high miscibility between DIP and PDIR−CN_2 molecules, forming a system wherein the two kinds of molecules are mixed without noticeable phase separation.[29] PHJ and SL GIXD profiles present a simple superposition of pristine film patterns (Figure S2).

Since PDIR−CN_2 is less ordered than DIP, we used thicker films (d = 100 nm for the pristine PDIR−CN_2 and 1:1) in order to obtain a better diffraction pattern. All reflections in the PDIR−CN_2 spectrum at q_{xy} values exceeding 0.76 $Å^{-1}$ can be assigned to the known crystal structure.[16] However, the peak at

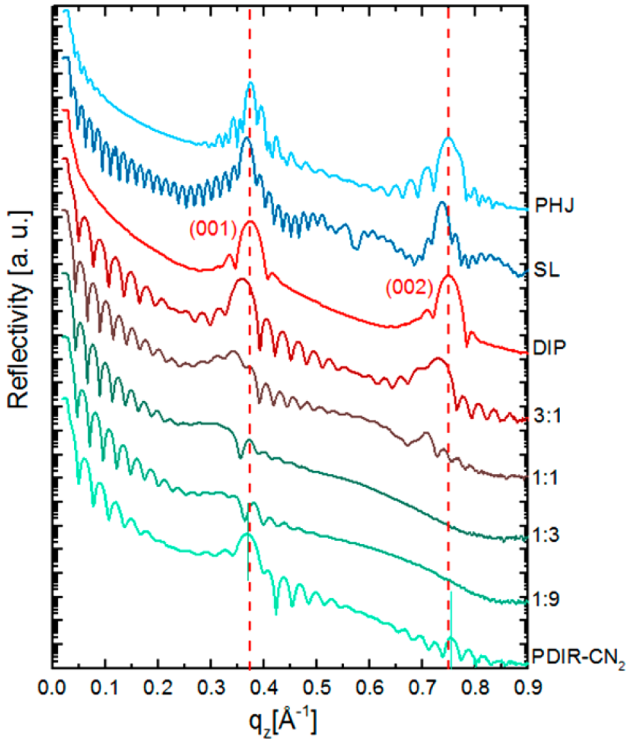

Figure 4. XRR data for DIP/PDIR−CN_2 coevaporated films and heterostructures. Dashed lines indicate the position of the 1st- and 2nd-order Bragg peak for DIP. The spectra are vertically offset for clarity.

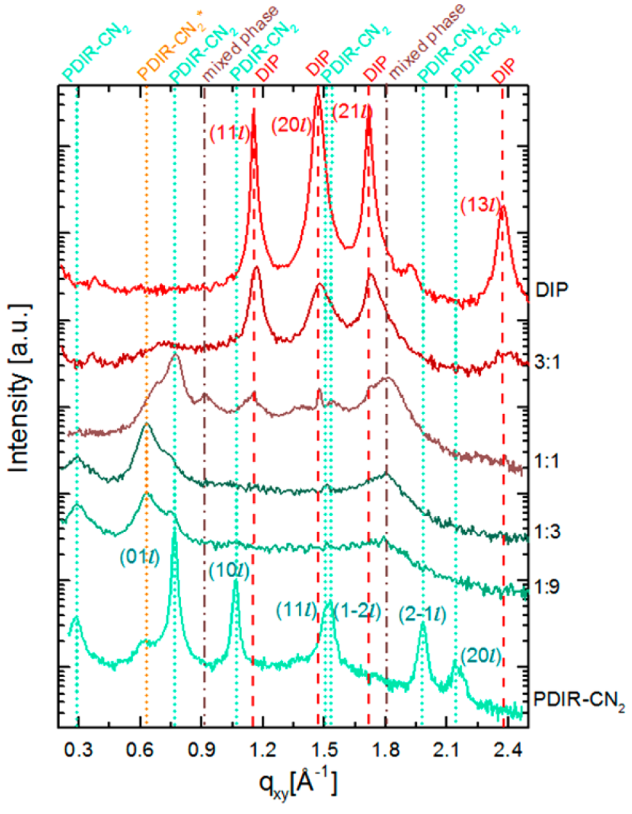

Figure 5. GIXD data of DIP/PDIR−CN_2 films for different mixing ratios. For better peak visibility in 1:1 and pristine PDIR−CN_2, 100 nm thick films were used. All spectra are vertically offset for clarity.

DOI: 10.1021/jacs.7b01622
J. Am. Chem. Soc. 2017, 139, 8474−8486

q_{xy} = 0.63 Å^{-1} does not originate from the known unit cell and stems from an unknown polymorph indicated as PDIR−CN_2*. Additional peaks are found in the equimolar mixed film at q_{xy} equal to 0.92 Å^{-1} and to 1.81 Å^{-1}. Because these two new reflections do not originate from the structures of the pure components, they are assigned to a new mixed phase polymorph. This observation indicates that the mixture is not completely random in the in-plane direction but has a preferred ordering, comparable to a cocrystal.[30,31] The corresponding coherent island size evaluated from the full-width at half-maximum (fwhm) l_s equals 3.5 nm, which is 5 times smaller than l_s in pristine films (18.8 nm for DIP and 18.4 nm for PDIR−CN_2). In the blends with predominant PDIR−CN_2 content, the pure polymorph PDIR−CN_2* is more pronounced. It shows phase separation from the mixed phase whereas in the 3:1 film, weak phase separation between DIP and the mixed phase occurs.

Since PDIR−CN_2 molecules (~22.0 Å) are longer than DIP molecules (~18.4 Å), and because in a cocrystal the axes of the π-conjugated cores should be parallel in the unit cell, the increase of the out-of-plane lattice spacing $d_{(001)}$ in blends is explained by a change of the PDIR−CN_2 molecular-tilt angle. The orientational changes of both compounds can be quantified by NEXAFS spectroscopy, which probes the average backbone orientation (for details see SI). The inclination angle of PDIR−CN_2 changes from 53 ± 5° in the pure film to 58 ± 5° in the 1:1 blend. Correspondingly, the DIP inclination angle changes from 79 ± 5° to 76 ± 5°.

Ground-State Properties. Having shown that both compounds are well intermixed and that the intermolecular electronic interaction is not inhibited by phase separation, we apply spectroscopic methods for its characterization. Using infrared (IR)-absorption spectroscopy, it is possible to assign a shift of intramolecular vibration frequencies to the degree of charge transfer between donor and acceptor in the absence of electronic excitation (i.e. in the electronic ground state). In particular, the stretching mode of the nitrile group (−C≡N) present in PDIR−CN_2 molecules is highly sensitive to CT.[32]

In Figure 6, we compare experimental IR spectra of pristine DIP and PDIR−CN_2, coevaporated equimolar DIP/PDIR−CN_2 films, calculated spectra of neutral PDIR−CN_2 in the gas phase, and of its radical anion. In the presented spectral range, DIP does not reveal any IR-active vibration modes, which makes the CN-mode ideal for comparison. The CN-stretching mode appears at ~2222 cm^{-1} (all peak positions are determined by using a Gaussian fit) in IR spectra of the pristine PDIR−CN_2 film. On the basis of our calculations, the CN-stretching mode of the PDIR−CN_2 radical anion reveals a red shift of 26 ± 2 cm^{-1} toward 2196 cm^{-1}. In the measured IR spectrum of the equimolar DIP/PDIR−CN_2 mixture, one can observe a red shift of the CN-mode peak of 4.5 ± 1 cm^{-1} (the instrumental resolution is 1 cm^{-1}). Assuming a linear correlation between charge transfer and the frequency shift of the CN-mode,[33] we can estimate that in the DIP/PDIR−CN_2 system, a partial charge transfer of about 0.17 ± 0.04 electrons occurs. This degree of interaction should be considered as non-negligible for the ground state, as it is comparable to other values for small-molecule CT complexes (e.g. 0.3 for TMP(tetramethoxypyrene)/TCNQ with ΔE_{DA} = 1−1.5 eV[34] or 0.12 for TMP/F_4−TCNQ with ΔE_{DA} = 0.6−1.1 eV).[35] For the PHJ sample, no shift is observed. In case of the superlattice, the peak that red-shifted by 2 cm^{-1} can be fitted with two Gaussians (Figure 6, dark blue curve), one unchanged and one

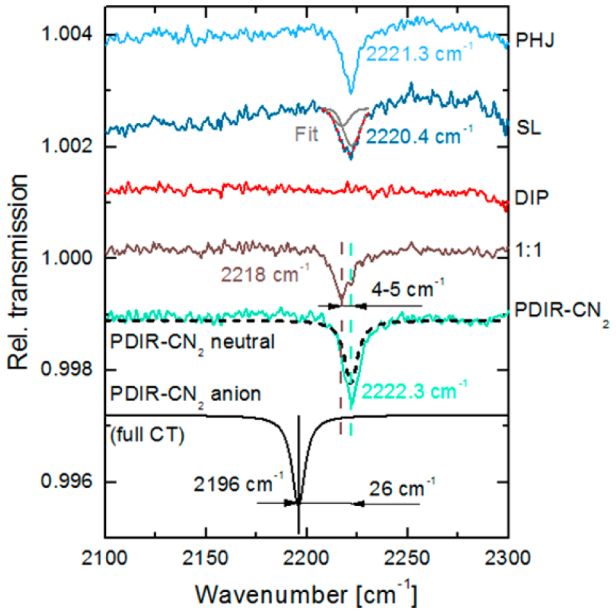

Figure 6. Infrared transmission of pristine DIP, PDIR−CN_2, equimolar mixture, heterostructures on silicon, and calculated spectra of neutral and ionized PDIR−CN_2 in gas phase. The spectra are vertically shifted for clarity. Peak positions are taken from a Gaussian fit.

shifted as in the blend, showing a smaller amount of interacting molecules.

Using ultraviolet photoelectron spectroscopy (UPS), we determined the HOMO-level onset and the work function of the molecular thin films, which are used to determine the ionization energies (IE). Part of the results is summarized in Figure 7. On weakly interacting, amorphous surfaces, such as SiO_2 or HIL 1.3-coated ITO, the DIP molecules grow almost upright standing, which results in IE = 5.40 eV.[36] The IE for pristine PDIR−CN_2 is 7.10 eV on SiO_2 substrates. For details on the orientation-dependent IE of DIP and PDIR−CN_2, see SI.

In the following, we discuss the energetic interplay at planar and mixed DIP/PDIR−CN_2 (D/A) interfaces. Looking at the PHJ architecture on ITO/HIL 1.3 as shown in Figure 7a, we observe Fermi-level pinning of DIP on HIL1.3, as shown before.[37] Upon subsequent deposition of PDIR−CN_2 on standing DIP molecules, we observe vacuum-level alignment between PDIR−CN_2 and DIP. The IE values for PDIR−CN_2 deposited on top of SiO_2 and on standing DIP molecules differ by ~0.35 eV. Taking the HOMO-level offset of 1.35 eV and a transport gap for PDIR−CN_2 of 2.65 eV, the energy gap ΔE_{DA} is about 1.3 eV. The transport gap taken for PDIR−CN_2 is estimated from the HOMO onset of a pristine PDIR−CN_2 film together with the observed Fermi level pinning of the LUMO at about −0.40 eV (for details see SI). This obtained transport gap is nearly identical to the one of DIP with 2.60 eV,[38] which is readily explained by the similarity of the π-conjugated cores and the optical gaps of both molecules. This also matches the measured transport gap of other perylene derivatives.[39]

The blended film of DIP and PDIR−CN_2 was evaporated on top of DIP-precovered ITO/HIL 1.3 substrates (Figure 7b). We observed a slight shift of the vacuum level, which is also reported for several other systems.[40,41] The HOMO onsets of the components were extracted from the deconvolution of the measured signal from the 100 Å-thick molecular blend (vertical

DOI: 10.1021/jacs.7b01622
J. Am. Chem. Soc. 2017, 139, 8474−8486

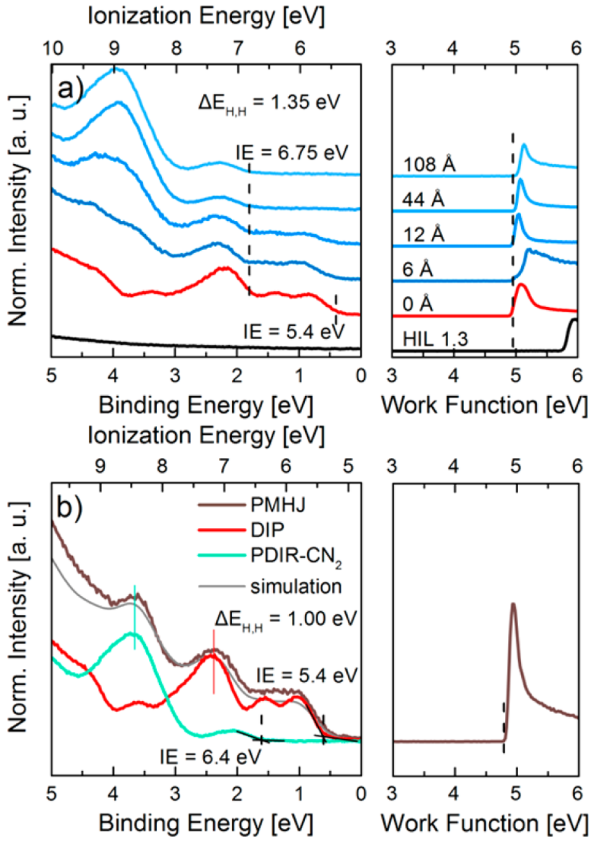

Figure 7. Valence-region spectra (left) and work-function measurements (right) of PHJ (a) and PMHJ (b) on HIL 1.3/ITO substrates for layers of increasing thicknesses. The HOMO and WF onset values are indicated by the vertical dashed lines. The red graphs show the baseline spectra of DIP-covered substrates. All spectra are scaled and shifted vertically for clarity. Part (b) shows the deconvolution of the valence band with pristine valence signatures for a 100 Å-thick film in PMHJ geometry. The green and red vertical lines are used to align the single-fit components. Further measurements are given in SI.

dashed lines, Figure 7b). The fit is a linear combination of two unaltered spectra of the pristine components and describes the measured spectrum well. In addition, the energetic positions of the single-fit components were kept fixed (green and red vertical lines) and a convolution with a Gaussian distribution (fwhm = 0.40 eV) was applied to account for spectral broadening due to increasing disorder in the mixed films as seen by X-ray scattering and AFM measurements. The disorder, along with the low sensitivity of the UPS setup itself, would explain the absence of new features for the weak CT complex here. At the planar mixed interface, ΔE_{DA} amounts to 1.65 eV, a further increase compared to the PHJ. The effect of the IE shift by intermixing was shown previously.[42,43]

The HOMO-level offset differs for the PHJ ($\Delta E_{H,H}^{PHJ}$ = 1.35 eV) and the PMHJ ($\Delta E_{H,H}^{PMHJ}$ = 1.00 eV) device architectures. This is related to differences of the energy levels in the two structures. Morphological changes, such as disorder, molecular reorientation, and mixing affect the electrostatic field at the thin-film surface and the coupling between the molecules.[41−45] Additionally, we find that a partial GS-CT shifts the HOMO levels as a whole but does not introduce a new feature in the UPS data. This finding contrasts with a HOMO-level offset between DIP and PDIR−CN_2 of 1.70 eV (which would give a smaller ΔE_{DA} of only 0.95 eV). This HOMO-level offset is expected from vacuum level alignment using the IEs for the pristine films.

Excited-State Properties. Now we studied if CT plays a role upon excitation, having already confirmed the presence of CT in the electronic ground state. Absorption spectra, taken by UV−vis−NIR spectroscopy, are shown in Figure 8a−c. Crystalline thin films of DIP and PDIR−CN_2 are expected to reveal anisotropic optical properties due to the transition dipole moment of the lowest electronic transition being oriented along the long molecular axis.[46] As the inclination angle of PDIR−CN_2 is smaller (~53°) compared to DIP (~83°), its absorption strength is, accordingly, higher in the in-plane direction (parallel to the substrate surface). The orientations of the transition dipole moments of individual molecules are depicted in Figure 2a,b. The positions of the energetically lowest peaks give the optical gap ΔE^{opt} of 2.25 eV for pristine DIP and 2.17 eV for pristine PDIR−CN_2. Compared with the transport gaps given above, 2.60 and 2.65 eV respectively, an exciton-binding energy of 0.4−0.5 eV can be derived.

Considering the spectrum of an equimolar blend, one can observe several features which can only be explained by taking into account the excited-state interaction between the two different compounds (see also the calculated superposition of the two pristine components, black curve in Figure 8b). As can be seen from Figure 8a, even a low concentration of DIP causes a rapid decrease in the intensity of the lowest PDIR−CN_2 peak at 2.17 eV (1:9 and 1:3). The intensity decrease of this transition in PDIR−CN_2 probably originates in the disturbed structural long-range order. Similarly, the DIP spectrum is influenced by intermixing with PDIR−CN_2 (3:1) as can be observed by the decrease of the peak intensity at 2.8 eV.[47]

As mentioned in the introduction, the observation of CT states in optical-absorption spectra often requires more sensitive techniques[48−53] because of the small cross section. However, the spectrum of the equimolar mixed film (1:1) clearly reveals a broad band at photon energies below the optical gaps of the pristine materials (1.4−2.1 eV, Figure 8c), which originates from direct excitation of CT states.[54−58] This subgap band, which is related to charge-transfer interaction,[59−61] was fitted using three Gaussian functions with peak positions at 1.58, 1.81, and 2.02 eV (fwhm: 0.25, 0.27, 0.20 eV). Together with a fourth Gaussian for the fundamental transition across the gap, the absorption spectrum in Figure 8c can be fitted over the whole measured range. Reasons for the observed splitting of the CT states may include variation in the unit cell or vibronic contributions. In contrast to the intermixed films, absorption spectra of PHJ and a superlattice (Figure 8b) are similar to a linear superposition of the spectra of the pristine materials, and a substantial contribution from CT states is absent.

Figure 8d shows photoluminescence spectra of single-component films and blended films with different mixing ratios recorded at low temperature (90 K) using an excitation energy of 2.33 eV. The DIP spectrum is in agreement with the literature.[62,63] PDIR−CN_2 reveals very strong emission intensities with two maxima at 1.69 and 1.84 eV at low temperature.

The emission intensity sharply decreases upon mixing and completely disappears in the equimolar blend within the range that of the pristine component. Moreover, one can observe a new peak emerging around 1.4 eV that reveals a slight red shift and increase in intensity with increasing PDIR−CN_2 fraction. We suggest to assign this new emission band to radiative

DOI: 10.1021/jacs.7b01622
J. Am. Chem. Soc. 2017, 139, 8474−8486

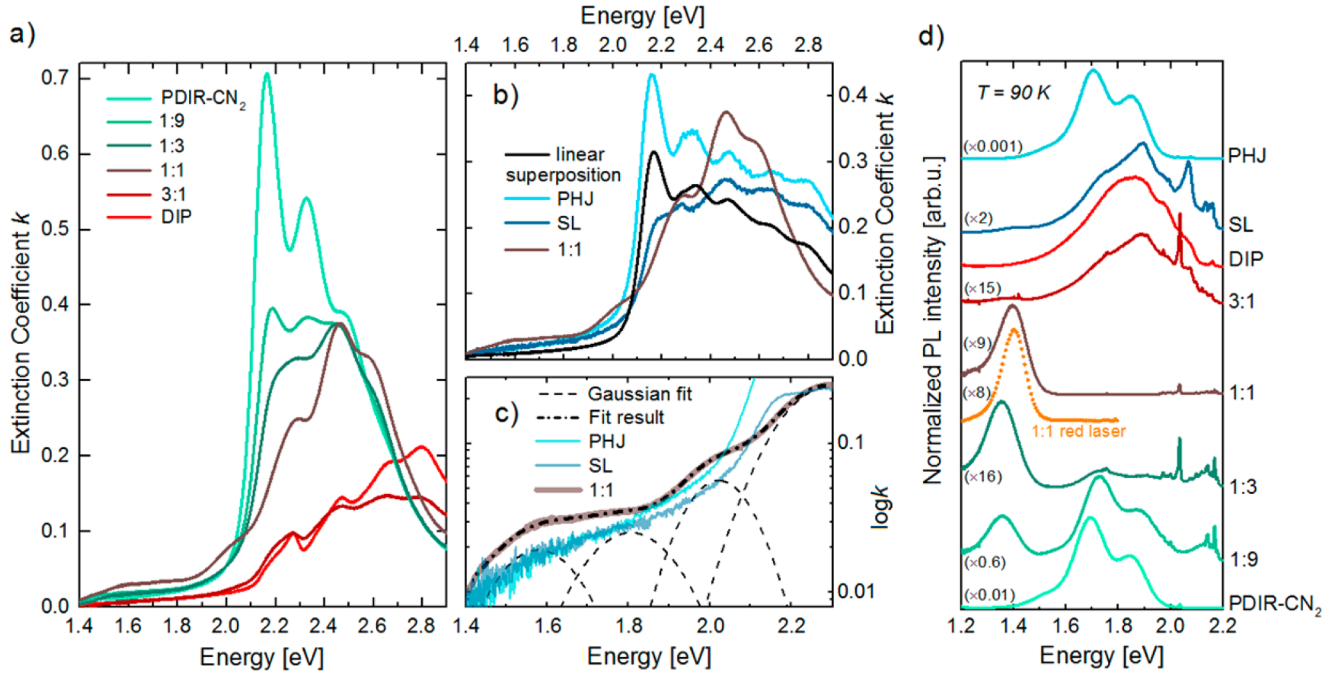

Figure 8. Absorption spectra for different mixing ratios (a) and heterostructures in comparison to the superposition of spectra from the pristine components (b). (c) Low-energy range plotted in logarithmic scale along the vertical axis with the CT absorption band decomposed into Gaussians for the results of the 1:1 film. (d) Low-temperature photoluminescence spectra recorded at 90 K.

recombination processes from the charge-transfer state between DIP and PDIR−CN_2 molecules.[57,64−66] In the equimolar blend, local exciton emission from the pristine compounds is almost quenched, which is consistent with a fully intermixed film. A similar effect was observed at low temperatures for other materials.[30,67] In addition, nonradiative recombination contributes much more strongly to the energy loss compared to the pristine materials, because the PL intensity observed in the 1:1 film is 1 order of magnitude weaker than in pristine DIP and three orders weaker than in pristine PDIR−CN_2. Using a red laser with an excitation energy of 1.96 eV, which is below the bandgap of the neat materials, the CT state can be excited directly, avoiding transfer from the higher-energy molecular excitons (Figure 8d).[57]

Regarding the layered samples, the PHJ exhibits strong emission especially at low temperatures mainly by PDIR−CN_2 excitonic recombination. As expected, emission from the SL contains features of both components, and only weak emission features from the CT states can be observed at 1.4 eV.

The recombination process through the CT state is further confirmed by time-resolved photoluminescence (TRPL) studies. The TRPL data presented in Figure 9 indicate that the strong long-lived emission of the singlet population of pristine DIP and PDIR−CN_2 at 10 K is quenched because of charge transfer at donor/acceptor interfaces. Thus, it decays on a shorter time scale of picoseconds in the mixed films. In addition, we observe clearly defined CT emission with a rise time shorter than the instrument response time (~15 ps), indicating that most of the CT states are actually populated on this time scale. The recorded PL dynamics in blends is thus dominated by CT emission. The effective $1/e$ decay times are shown in Table 1. The subnanosecond range has been typically observed for CT-emission decay.[68,69] For the blends with excess PDIR−CN_2, the CT state dynamics are not substantially altered when the temperature is varied between 10 and 290 K.

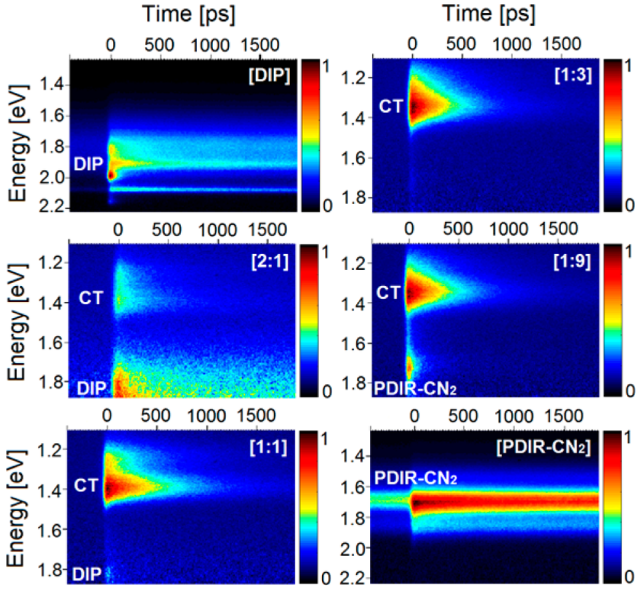

Figure 9. Two-dimensional plots of the spectrally and time-resolved PL signatures at 10 K for DIP/PDIR−CN_2 blends with varying mixing ratios, as labeled. The PL intensity is normalized to unity for each image. Weak signatures of DIP and PDIR−CN_2 are observed in the blends beside the more dominant and long-lived CT peak. At low temperatures, there is a pre-edge emission at negative delay times in the pristine films as a result of a long lifetime (>12.5 ns).

They show clear monoexponential decays (see SI) with no evidence for side decay processes such as singlet exciton dissociation, which is expected to occur in the shorter time range.[12,69] In the case of the 1:1 blend, however, the PL decay becomes faster with increasing temperature, indicating the presence of a thermally activated quenching mechanism. Such quenching could be either resulting from the thermally

DOI: 10.1021/jacs.7b01622
J. Am. Chem. Soc. 2017, 139, 8474−8486

Table 1. Effective Decay Times Extracted from Monoexponential Fits of PL Transients Recorded at Low and Room Temperatures

material	τ at 10 K	τ at 290 K
DIP	>12.5 ns	257 ps
2:1	190 ps	182 ps
1:1	496 ps	342 ps
1:3	448 ps	418 ps
1:9	452 ps	433 ps
PDIR−CN_2	>12.5 ns	151 ps

activated dissociation of CT states, or emerge from the presence of nonradiative recombination centers. However, thermally activated CT dissociation would require binding energies on the order of k_BT, which is much smaller than the value of 0.2 eV evaluated in the following (see Discussion), whereas the hypothesis of nonradiative recombination centers would imply a certain mobility of CT states with a temperature-dependent diffusion coefficient.[70]

From the comparison of intermixed and layered samples, where the CT signatures are only weakly present, one can assume an anisotropic character of the CT transitions polarized in the in-plane direction. In order to explore the anisotropy in detail, we performed variable-angle spectroscopic ellipsometry (VASE)[25] on a film with the most pronounced CT effect, that is the 1:1 ratio (ellipsometry data for the other mixing ratios are given in SI). The in-plane and out-of-plane components of the extinction coefficient are presented in Figure 10. The CT band

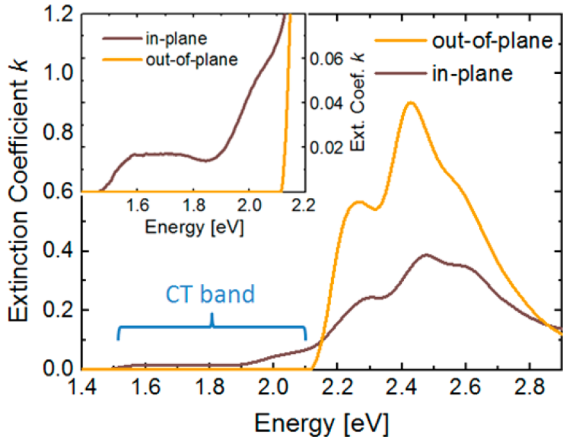

Figure 10. Anisotropic components of the extinction coefficient k of the 1:1 film. The inset zooms into the range of 1.4−2.2 eV. The in-plane component corresponds to the absorption data in Figure 8.

between 1.5−2.1 eV is only visible in the in-plane direction, which is the direction of the $\pi-\pi$ interaction. This result is consistent with the absence of the CT transition in the PHJ and the SL, where no significant $\pi-\pi$ stacking of both compounds is present, and it is also in agreement with CT transitions in other compounds.[71]

To complete the optical characterization by absorption and photoluminescence spectra, we also measured electroluminescence (EL) and the incident-photon-to-current efficiency (IPCE) spectra of solar cells. The recorded IPCE spectra (see Figure 11) display significant differences between PHJ and PMHJ cell architectures. Note that while the IPCE data in the subgap region (<2 eV) correlate very well with the absorption spectra of the 1:1 blend and the PDIR−CN_2/DIP bilayer

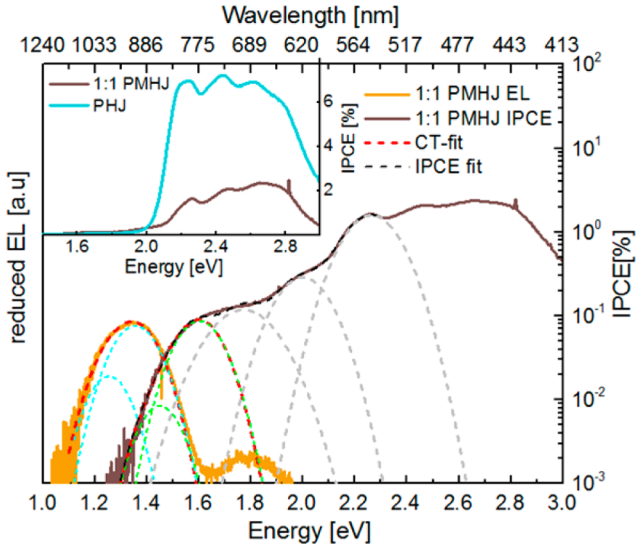

Figure 11. The orange curve represents the reduced EL spectrum of the 1:1 PMHJ sample measured at a 3 V bias voltage. The brown line shows the IPCE spectrum of the 1:1 PMHJ solar cell. The red dashed lines show the superposition of Gaussians corresponding to the CT-fit, which are light-blue and light-green for EL- and IPCE-fit, respectively. The gray dashed lines complete the light-green Gaussians to the IPCE-fit over the whole CT range (black dashed line). Note that the peak at 2.25 eV belongs to the pristine material. The inset displays linear-scaled IPCE measurements of PHJ and PMHJ cells. The sharp peak around 2.8 eV (IPCE of PMHJ cell) is a measurement artifact. All spectra were recorded at 297 K.

displayed in Figure 8b,c, there is a distinct difference in the spectral range above the gap (2−3 eV). In this spectral region, the PHJ device exhibits a 2- to 3-fold greater photocurrent as compared to the PMHJ device. The lower current of the latter cannot be fully explained by the lower absorptivity of the blend with respect to the bilayer structure (see Figure 8b), which results from a less-favorable molecular orientation for light absorption. Instead, the lower current indicates that the PMHJ suffers from a charge-transport problem because of the intimate intermixing of DIP and PDIR−CN_2 in the 1:1 blend. Because of the good miscibility of both components, there are no separate percolation paths for the extraction of the generated charge-carrier pairs, which are trapped and subsequently recombine in the mixed phase (see also the discussion on charge transport in the following section and ref[72]). However, even in the PHJ device the IPCE stays below 10%, mainly because of insufficient light absorption resulting from the predominantly standing orientation of both molecular species.

In the logarithmic representation, Figure 11 shows EL spectra of a PMHJ device that was operated as a light-emitting diode (LED) under a forward bias of 3 V. The luminescence signal was normalized to the maximum at about 1.35 eV, which corresponds well to the CT-emission band observed in photoluminescence spectra of the blends (see Figure 8d). In addition, there is a much weaker band at about 1.8 eV, which could stem from luminescence of one of the pristine materials. For the PHJ device, there was no detectable EL emission in the calibrated wavelength range (300−1000 nm), even at a voltage as high as 4.5 V, where the devices are close to failure. In contrast to the PL spectra shown in Figure 8d, we do not see emission from the pristine materials in a PHJ, which indicates that nearly all injected electron−hole pairs recombine at the D/A interface. However, the radiative efficiency of emission from

DOI: 10.1021/jacs.7b01622
J. Am. Chem. Soc. 2017, 139, 8474−8486

CT states polarized in the out-of-plane direction seems to be extremely small.

As introduced by Tvingstedt et al.[51] and refined by Vandewal et al.,[73] EL and IPCE spectra can be analyzed in the framework of Marcus theory to estimate the CT energy E_{CT}, which can then be discussed in relation to the open-circuit voltage V_{OC} of the solar cells to quantify energy losses.[18,74] As the EL data show an asymmetric peak, we modified the CT approach and fitted our data with the sum of two Gaussians (CT-fit, see Figure 11). Both the reduced absorption $\sum_{i=1}^{2}\sigma_i(E)E$ and the reduced emission $\sum_{i=1}^{2} I_{f,i}(E)E^{-1}$ were fitted with

$$\left.\begin{aligned}&\sum_{i=1}^{2}\sigma_i(E)E\\&\sum_{i=1}^{2} I_{f,i}(E)E^{-1}\end{aligned}\right\} = = \sum_{i=1}^{2}\frac{f_{\sigma_i, I_{f,i}}}{\sqrt{4\pi\lambda_{0,i}k_BT}}\exp\left(\frac{-(E_{CT,i}\pm\lambda_{0,i}-E)^2}{4\lambda_{0,i}k_BT}\right)$$

Here, λ_0 represents the reorganization energy related to the Stokes shift in the CT manifold. Variables f_σ and f_{I_f} are proportional to the square of the electronic-coupling matrix element. The plus and the minus sign are taken for reduced absorption and reduced emission, respectively. Consequently, we obtain two different CT energies: E_{CT1} = 1.35 eV and E_{CT2} = 1.48 eV, with the latter value stemming from the peak with the stronger spectral weight. This energy splitting may stem from structural variations or a vibronic progression.

In order to confirm the superposition of different CT states included in the absorption band, we fitted the IPCE spectra (as in Figure 8c) with the sum of Gaussians as shown in Figure 11 on the right axis. Although the absorption CT band consists of at least four distinct states, obviously only two of them lead to radiative recombination. Similar behavior has been observed in the literature for systems with a spectrally broad manifold of CT states.[75,76] However, whereas this can be seen as evidence for energetic relaxation in the CT density of states, there still remains the question of whether equilibrium is reached within the lifetime of carriers. Further investigations will have to clarify this issue.

Device Behavior. To elucidate the mechanisms of charge separation and transport, photoelectrical measurements were performed for solar cells built in the PHJ and PMHJ (1:1) device architectures. This allows for a direct comparison of the photocurrent and the open-circuit voltage between face-to-face (in-plane) and edge-on-edge (out-of-plane) stacking.

The solar cell architecture can be seen in Figure 12 alongside the $j-V$ characteristics of PHJ and PMHJ solar cells in dark (dashed lines) and under one sun simulated AM1.5G illumination (solid lines). The solar-cell parameters extracted from $j-V$ measurements are collected in Table 2. Note that the open-circuit voltage (V_{OC}) of both architectures is equal and amounts to 0.50 V, whereas the short-circuit current changes significantly from −0.65 mA/cm^2 for the PHJ to −0.24 mA/cm^2 for the PMHJ cell, which correlates very well with the IPCE results. The fill factor (FF) decreases from 57% (PHJ) to 40% (PMHJ). As a result, the efficiency is reduced from 0.18% for the PHJ to 0.05% for the PMHJ cell. This contrasts with phase-separating mixtures, where PMHJ cells provide higher

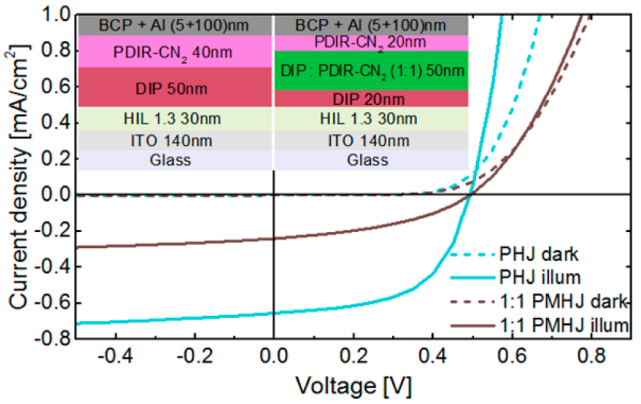

Figure 12. $j-V$ diagram of PHJ and PMHJ DIP/PDIR−CN_2 based solar cells. Dashed lines represent measurements in the dark and the solid lines under illumination. The inset shows the stack architecture of the PHJ (left) and PMHJ (right) solar cells.

Table 2. Solar Cell Parameters Extracted From $j-V$ Characteristics of PHJ and PMHJ solar cells Recorded Under Illumination[a]

config.	V_{OC} (V)	j_{sc} (mA/cm^2)	FF(%)	η(%)
PHJ	0.50	−0.65	57	0.18
PMHJ	0.50	−0.24	40	0.05

[a]Corresponding $j-V$ curves are shown in Figure 12.

efficiencies than their PHJ counterparts.[37] Thus, some degree of phase separation, as opposed to perfect intermixing, is beneficial for charge separation in order to increase the device performance.

In general, the open-circuit voltage of an organic molecular D/A solar cell can be written as[18,74]

$$V_{OC}(T) = \frac{E_{CT}}{q} - \Delta V_{OC}$$

where q is the elementary charge, and E_{CT} sets the upper limit of V_{OC}, which can be achieved only in the low-temperature limit. At a finite temperature, there is an energy loss $q\Delta V_{OC} = q\Delta V_{OC}^{rad} + q\Delta V_{OC}^{nonrad}$, composed of thermodynamically inevitable radiative losses as well as nonradiative losses. For a wide range of organic D/A systems, the energy loss between E_{CT} and the V_{OC} at 300 K is in the range of 0.5−0.6 eV.[9,72] In our case, from E_{CT2}= 1.48 eV for the dominant optically detected CT state, we obtain an energy loss of $q\Delta V_{OC}$ of about 1 eV, significantly larger than the typically observed range.

Furthermore, the photovoltaic gap ΔE_{DA} from UPS is an additional measure for the V_{OC} limit in solar cells and was used before to estimate losses in V_{OC} in PHJ solar cells.[77] For the planar heterojunction of DIP/PDIR−CN_2, the ΔE_{DA} is 1.3 eV. Therefore, the losses for the open-circuit voltage regarding the energy-level offset amount to ∼0.8 V, larger than for previously analyzed material combinations.[77] As discussed in the previous section, the reason for the high energy losses and the low V_{OC} (and as a consequence for the low overall efficiencies) observed for both cell architectures could lie in the broad manifold of CT states with energy relaxation toward the lowest states from where only weak radiative recombination is observed.

In addition to j-V measurements on solar cells, we also determined the electrical conductivity in the dark σ_{dark} of pristine and blended films for varying molar doping ratios. The results are shown in Figure 13. Both pristine materials are

DOI: 10.1021/jacs.7b01622
J. Am. Chem. Soc. 2017, 139, 8474−8486

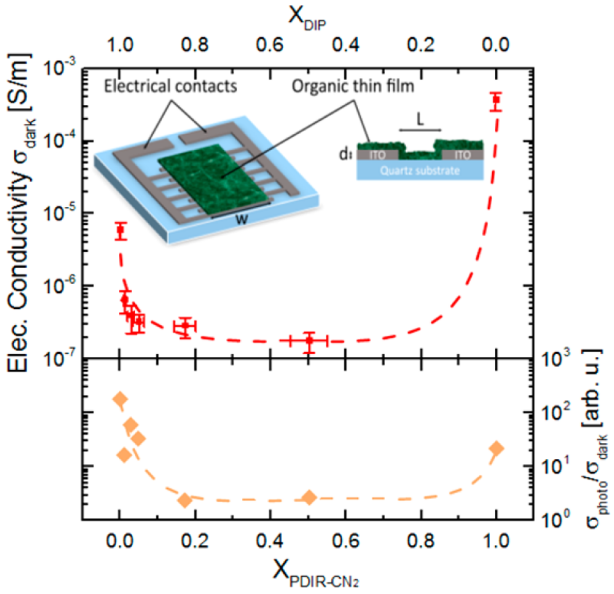

Figure 13. Electrical conductivity σ depending on the relative molecular concentration of PDIR−CN_2 to DIP is shown in the top panel. In the bottom panel, the ratio between electrical conductivity under illumination and dark conditions $\sigma_{photo}/\sigma_{dark}$ is shown. The dashed lines serve as a guide to the eye.

reported to form films with high mobility, DIP for holes and electrons, and PDIR−CN_2 only for electrons.[78,79] In the heterostructures, σ_{dark} decreases by adding the other compound, which is readily explained by the altered crystal structure compared to both pristine materials and, as a consequence, lower ordering.[80] This minimum in σ_{dark} is reached around equimolar mixing ratios. Additionally, we recorded the electrical conductivity under illumination to look at the photoconductivity of the blended system. The ratio of σ_{photo} to σ_{dark} is shown in Figure 13 (bottom panel). The strong decrease in the ratio of σ_{photo} to σ_{dark} supports the beforementioned discussion on the photocurrent in solar cells. A similar conductivity decrease in molecular blends by dilution has been observed earlier.[72,81,82]

As a result of the intimate mixture of the molecules in the blended films, high recombination losses and charge trapping are present. This results in low conductivities of blended films together with the absence of increased conductivities under illumination in these films. These effects are limiting the overall performance of the PMHJ solar cells, as discussed before.

Discussion. The presence of a CT interaction between donor and acceptor materials has recently attracted attention because of its importance for organic solar cells and organic light-emitting diodes[83] as well as the associated fundamental challenges. It was shown that the CT energy can serve as a limit for the open-circuit voltage in solar cells.[73,84] However, even if the resulting exciton has charge-transfer character, ground-state interactions are still present.[61,85]

The two perylene derivatives DIP and PDIR−CN_2 are an excellent model system to study CT effects in organic semiconductors. Mixtures are well ordered in the out-of-plane direction, which means each molecule has a well-defined inclination angle to the substrate. In the in-plane direction, mixed films have a small coherent island size but nevertheless exhibit preferential D/A stacking, which enables the CT state formation in this direction. Intermolecular D/A interactions are directly related to the overlap of their frontier orbitals, which is maximal in $\pi-\pi$ stacking or face-to-face geometry. Therefore, the presented CT is stronger in mixed films (BHJ and PMHJ), where the molecule reorientation facilitates orbital overlap, in contrast to planar interfaces (PHJ and SL) with almost exclusively edge-on-edge stacking.

We observed a partial charge transfer in the ground state of 0.17 electrons, as determined from IR spectroscopy and DFT calculations. This leads to a shift of the HOMO levels of both compounds toward each other. Judging from UPS data, we find that the HOMO-level offset in the mixture is only 1.00 eV in contrast to the 1.70 eV expected from the vacuum-level alignment. Although we found this relatively strong shift in the HOMO levels, there are no hints for new states or orbital hybridization in the ground state, because the mixed film valence region spectrum is just a superposition of the pristine film spectra taking into account the change of IE. The opposite is true for the excited state, where we observe new states via UV−vis−NIR absorption spectroscopy and PL/EL spectroscopies. The resulting energy diagram for mixed films is presented in Figure 14, where the energy gap ΔE_{DA} of 1.65

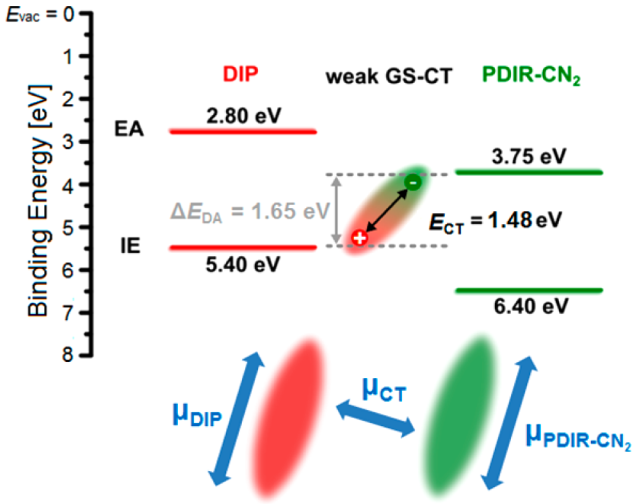

Figure 14. Schematic energy-level diagram for the mixture DIP/PDIR−CN_2 (top) and orientations of transition dipole moments (bottom). IE values were determined by UPS, the EA values by subtracting the transport gaps from IE values. E_{CT} is taken from the strong CT energy, calculated from the EL and IPCE data. ΔE_{DA} is the difference between the DIP IE and the PDIR−CN_2 EA.

eV and the dominant CT state of 1.48 eV give a CT exciton-binding energy of about 0.2 eV. This is smaller than the exciton-binding energy of the pristine materials (0.4−0.5 eV). The lower exciton-binding energy of the CT state can be explained by the wider charge separation compared to the exciton associated with the first HOMO−LUMO transition in the pristine materials.[86,87]

For many photovoltaic material combinations, highly sensitive methods are necessary to measure the weak CT transitions. However, for the case presented here, some of the strong CT absorptions are detectable with standard UV−vis−NIR absorption spectroscopy. Furthermore, the CT absorption is present not only close to the absorption edge of the pristine materials, but it has a rather broad energy range of about 0.6 eV. We also find a corresponding feature in photoluminescence and electroluminescence at 1.4 eV with a strong quenching of

DOI: 10.1021/jacs.7b01622
J. Am. Chem. Soc. 2017, 139, 8474−8486

emission from the single components. The drastic change of molecular absorption and emission spectra provides strong evidence for the formation of a D/A complex with new electronic properties. Time-resolved PL reveals that the CT state lifetime of 400−500 ps is significantly shorter compared to the individual compounds at 10 K and nearly independent from temperature. Judging from this, the CT states open the dominant recombination channel.

Importantly, our findings demonstrate the anisotropic character of the electronic transition to the excited CT state. As sketched in Figure 14 (bottom), it is strong in the in-plane direction, where $\pi-\pi$ intermolecular stacking occurs (perpendicular to the molecular backbones), but absent between molecules in the edge-on-edge configuration. Thus, $\pi-\pi$ stacking is a prerequisite for the efficient intermolecular coupling, which is the main characteristic for GS-CT (Figure 1). If an intimately mixed structure is established, further properties of the formed complex are primarily determined by the energy level difference ΔE_{DA}, which in our case amounts to 1.65 eV. This is apparently too high for a substantial hybridization of the molecular orbitals. By considering the structural prerequisite of molecules to form $\pi-\pi$ stacking and the magnitude of ΔE_{DA}, one may make a prediction for the interaction type that a D/A combination will exhibit. We note further that the anisotropic character of CT is not in contradiction with our observation of equal V_{OC} for PHJ and PMHJ solar cell configurations, because the rough polycrystalline DIP layer shown in Figure 3 offers enough surface area for $\pi-\pi$ stacking with PDIR−CN_2 molecules even in a PHJ. Thus, the equality of the observed V_{OC}s underlines the dominance of the energetically favorable face-to-face CT recombination pathway.

The formation of coupled but weakly ordered crystalline D/A complexes, where excited CT states serve as traps for excitons[72,81,82] and open pathways for radiative and nonradiative recombination, is accompanied by a decrease of charge-carrier conductivity and an increase of energy losses. Nevertheless, material combinations with strong CT absorption could lead to increased short-circuit current by using more photons from the infrared region. The overall efficiency could be increased by using well-ordered mixed-stack charge-transfer crystals because of an improved extraction efficiency[13,88,89] and applying them as donor and/or acceptor in photovoltaic cells. Combining the higher degree of structural order, the broad CT absorption and reduced energy losses might lead to new device architectures.

SUMMARY

In summary, a comprehensive study of an organic D/A molecular system (DIP/PDIR−CN_2) prepared by OMBD involving structural, optical, electronic, and device characterization has been performed. We have identified the formation of a CT complex characterized by a weak ground-state interaction expressed in a partial CT of 0.17 electrons per molecule and a strong excited-state CT, which is highly anisotropic in nature. The strong intermolecular coupling together with the intimately mixed structure without phase separation contributes to the large energy losses in solar cells from these materials.

ASSOCIATED CONTENT

Supporting Information

The Supporting Information is available free of charge on the ACS Publications website at DOI: 10.1021/jacs.7b01622.

AFM surface profiles, film parameters extracted from XRR fit, GIXD scans for heterostructure samples, details on UPS, NEXAFS data, TRPL transients, the full ellipsometry data sets (PDF)

AUTHOR INFORMATION

Corresponding Authors

*valentina.belova@uni-tuebingen.de
*frank.schreiber@uni-tuebingen.de
*wolfgang.bruetting@physik.uni-augsburg.de
*andreas.opitz@hu-berlin.de

ORCID

Valentina Belova: 0000-0002-8142-2090

Notes

The authors declare no competing financial interest.

ACKNOWLEDGMENTS

We thank the European Synchrotron Radiation Facility (ESRF), Grenoble, France, for enabling X-ray diffraction experiments at beamline ID10, and the Paul Scherrer Institut, Villigen, Switzerland, for providing synchrotron radiation beamtime at MS-Surf-Diffr X04SA of the Swiss Lightsource (SLS). We also thank Nicola Casati for assistance. We are grateful for beamtime at the synchrotron storage ring BESSY II at Helmholtz-Zentrum Berlin (beamlines PM4 and UE52) as well as to the MAX IV laboratory, Lund, Sweden, with storage ring MAX II and beamline D1011. We gratefully acknowledge financial support of the Deutsche Forschungsgemeinschaft (SCHR 700/20-1, Br 1728/14-1, OP 159/2-1, SFB 1083).

REFERENCES

(1) Tang, C. W. *Appl. Phys. Lett.* **1986**, *48*, 183−185.
(2) Brédas, J.-L.; Norton, J. E.; Cornil, J.; Coropceanu, V. *Acc. Chem. Res.* **2009**, *42*, 1691−1699.
(3) Tang, C. W.; VanSlyke, S. A. *Appl. Phys. Lett.* **1987**, *51*, 913−915.
(4) Friend, R. H.; Gymer, R. W.; Holmes, A. B.; Burroughes, J. H.; Marks, R. N.; Taliani, C.; Bradley, D. D. C.; Dos Santos, D. A.; Brédas, J. L.; Lögdlund, M.; Salaneck, W. R. *Nature* **1999**, *397*, 121−128.
(5) Mulliken, R. S. *J. Phys. Chem.* **1952**, *56*, 801−822.
(6) Linderl, T.; Hörmann, U.; Beratz, S.; Gruber, M.; Grob, S.; Hofmann, A.; Brütting, W. *J. Opt.* **2016**, *18*, 24007.
(7) Bartynski, A. N.; Grob, S.; Linderl, T.; Gruber, M.; Brütting, W.; Thompson, M. E. *J. Phys. Chem. C* **2016**, *120*, 19027−19034.
(8) Bartynski, A. N.; Gruber, M.; Das, S.; Rangan, S.; Mollinger, S.; Trinh, C.; Bradforth, S. E.; Vandewal, K.; Salleo, A.; Bartynski, R. A.; Bruetting, W.; Thompson, M. E. *J. Am. Chem. Soc.* **2015**, *137*, 5397−5405.
(9) Hörmann, U.; Kraus, J.; Gruber, M.; Schuhmair, C.; Linderl, T.; Grob, S.; Kapfinger, S.; Klein, K.; Stutzman, M.; Krenner, H. J.; Brütting, W. *Phys. Rev. B: Condens. Matter Mater. Phys.* **2013**, *88*, 235307.
(10) Bredas, J.-L. *Mater. Horiz.* **2014**, *1*, 17.
(11) Aghamohammadi, M.; Fernández, A.; Schmidt, M.; Pérez-Rodríguez, A.; Goñi, A. R.; Fraxedas, J.; Sauthier, G.; Paradinas, M.; Ocal, C.; Barrena, E. *J. Phys. Chem. C* **2014**, *118*, 14833−14839.
(12) Bernardo, B.; Cheyns, D.; Verreet, B.; Schaller, R. D.; Rand, B. P.; Giebink, N. C. *Nat. Commun.* **2014**, *5*, 3245.
(13) Méndez, H.; Heimel, G.; Winkler, S.; Frisch, J.; Opitz, A.; Sauer, K.; Wegner, B.; Oehzelt, M.; Röthel, C.; Duhm, S.; Többens, D.; Koch, N.; Salzmann, I. *Nat. Commun.* **2015**, *6*, 8560.

DOI: 10.1021/jacs.7b01622
J. Am. Chem. Soc. 2017, 139, 8474−8486

(14) Salzmann, I.; Heimel, G.; Duhm, S.; Oehzelt, M.; Pingel, P.; George, B. M.; Schnegg, A.; Lips, K.; Blum, R.-P.; Vollmer, A.; Koch, N. *Phys. Rev. Lett.* **2012**, *108*, 035502.
(15) Mahns, B.; Kataeva, O.; Islamov, D.; Hampel, S.; Steckel, F.; Hess, C.; Knupfer, M.; Büchner, B.; Himcinschi, C.; Hahn, T.; Renger, R.; Kortus, J. *Cryst. Growth Des.* **2014**, *14*, 1338−1346.
(16) Ferlauto, L.; Liscio, F.; Orgiu, E.; Masciocchi, N.; Guagliardi, A.; Biscarini, F.; Samorì, P.; Milita, S. *Adv. Funct. Mater.* **2014**, *24*, 5503−5510.
(17) Zhou, Y.; Taima, T.; Kuwabara, T.; Takahashi, K. *Adv. Mater.* **2013**, *25*, 6069−6075.
(18) Gruber, M.; Wagner, J.; Klein, K.; Hörmann, U.; Opitz, A.; Stutzmann, M.; Brütting, W. *Adv. Energy Mater.* **2012**, *2*, 1100−1108.
(19) Lee, J.; Jadhav, P.; Reusswig, P. D.; Yost, S. R.; Thompson, N. J.; Congreve, D. N.; Hontz, E.; Van Voorhis, T.; Baldo, M. A. *Acc. Chem. Res.* **2013**, *46*, 1300−1311.
(20) Schreiber, F. *Phys. status solidi* **2004**, *201*, 1037−1054.
(21) Witte, G.; Wöll, C. *J. Mater. Res.* **2004**, *19*, 1889−1916.
(22) Nečas, D.; Klapetek, P. *Open Phys.* **2012**, *10*, 181−188.
(23) Björck, M.; Andersson, G. *J. Appl. Crystallogr.* **2007**, *40*, 1174−1178.
(24) Parratt, L. G. *Phys. Rev.* **1954**, *95*, 359−369.
(25) Heinemeyer, U.; Hinderhofer, A.; Alonso, M. I.; Ossó, J. O.; Garriga, M.; Kytka, M.; Gerlach, A.; Schreiber, F. *Phys. Status Solidi A* **2008**, *205*, 927−930.
(26) Dürr, A. C.; Schreiber, F.; Ritley, K. A.; Kruppa, V.; Krug, J.; Dosch, H.; Struth, B. *Phys. Rev. Lett.* **2003**, *90*, 16104.
(27) Kowarik, S.; Gerlach, A.; Sellner, S.; Schreiber, F.; Cavalcanti, L.; Konovalov, O. *Phys. Rev. Lett.* **2006**, *96*, 125504.
(28) Hinderhofer, A.; Hosokai, T.; Frank, C.; Novák, J.; Gerlach, A.; Schreiber, F. *J. Phys. Chem. C* **2011**, *115*, 16155−16160.
(29) Hinderhofer, A.; Schreiber, F. *ChemPhysChem* **2012**, *13*, 628−643.
(30) Hinderhofer, A.; Frank, C.; Hosokai, T.; Resta, A.; Gerlach, A.; Schreiber, F. *J. Chem. Phys.* **2011**, *134*, 104702.
(31) Dieterle, J.; Broch, K.; Hinderhofer, A.; Frank, H.; Novák, J.; Gerlach, A.; Breuer, T.; Banerjee, R.; Witte, G.; Schreiber, F. *J. Phys. Chem. C* **2015**, *119*, 26339−26347.
(32) Chappell, J. S.; Bloch, A. N.; Bryden, W. A.; Maxfield, M.; Poehler, T. O.; Cowan, D. O. *J. Am. Chem. Soc.* **1981**, *103*, 2442−2443.
(33) Nanova, D.; Beck, S.; Fuchs, A.; Glaser, T.; Lennartz, C.; Kowalsky, W.; Pucci, A.; Kroeger, M. *Org. Electron.* **2012**, *13*, 1237−1244.
(34) Rudloff, M.; Ackermann, K.; Huth, M.; Jeschke, H. O.; Tomic, M.; Valentí, R.; Wolfram, B.; Bröring, M.; Bolte, M.; Chercka, D.; Baumgarten, M.; Müllen, K. *Phys. Chem. Chem. Phys.* **2015**, *17*, 4118−4126.
(35) Medjanik, K.; Perkert, S.; Naghavi, S.; Rudloff, M.; Solovyeva, V.; Chercka, D.; Huth, M.; Nepijko, S. A.; Methfessel, T.; Felser, C.; Baumgarten, M.; Müllen, K.; Elmers, H. J.; Schönhense, G. *Phys. Rev. B: Condens. Matter Mater. Phys.* **2010**, *82*, 245419.
(36) Han, W. N.; Yonezawa, K.; Makino, R.; Kato, K.; Hinderhofer, A.; Murdey, R.; Shiraishi, R.; Yoshida, H.; Sato, N.; Ueno, N.; Kera, S. *Appl. Phys. Lett.* **2013**, *103*, 253301.
(37) Wagner, J.; Gruber, M.; Hinderhofer, A.; Wilke, A.; Bröker, B.; Frisch, J.; Amsalem, P.; Vollmer, A.; Opitz, A.; Koch, N.; et al. *Adv. Funct. Mater.* **2010**, *20*, 4295−4303.
(38) Krause, S.; Schöll, A.; Umbach, E. *Org. Electron.* **2013**, *14*, 584−590.
(39) Arantes, C.; Scholz, M.; Schmidt, R.; Dehm, V.; Rocco, M. L. M.; Schöll, A.; Reinert, F.; Würthner, F. *Appl. Phys. A: Mater. Sci. Process.* **2012**, *108*, 629−637.
(40) Opitz, A.; Frisch, J.; Schlesinger, R.; Wilke, A.; Koch, N. *J. Electron Spectrosc. Relat. Phenom.* **2013**, *190*, 12−24.
(41) Akaike, K.; Koch, N.; Heimel, G.; Oehzelt, M. *Adv. Mater. Interfaces* **2015**, *2*, 1500232.
(42) Schwarze, M.; Tress, W.; Beyer, B.; Gao, F.; Scholz, R.; Poelking, C.; Ortstein, K.; Günther, A. A.; Kasemann, D.; Andrienko, D.; Leo, K. *Science* **2016**, *352*, 1446−1449.
(43) Salzmann, I.; Duhm, S.; Heimel, G.; Oehzelt, M.; Kniprath, R.; Johnson, R. J.; Rabe, J. P.; Koch, N. *J. Am. Chem. Soc.* **2008**, *130*, 12870−12871.
(44) Heimel, G.; Salzmann, I.; Duhm, S.; Koch, N. *Chem. Mater.* **2011**, *23*, 359−377.
(45) Duhm, S.; Heimel, G.; Salzmann, I.; Glowatzki, H.; Johnson, R. L.; Vollmer, A.; Rabe, J. P.; Koch, N. *Nat. Mater.* **2008**, *7*, 326−332.
(46) Heinemeyer, U.; Scholz, R.; Gisslén, L.; Alonso, M. I.; Ossó, J. O.; Garriga, M.; Hinderhofer, A.; Kytka, M.; Kowarik, S.; Gerlach, A.; Schreiber, F. *Phys. Rev. B: Condens. Matter Mater. Phys.* **2008**, *78*, 085210.
(47) Heinemeyer, U.; Broch, K.; Hinderhofer, A.; Kytka, M.; Scholz, R.; Gerlach, A.; Schreiber, A. *Phys. Rev. Lett.* **2010**, *104*, 257401.
(48) Osterloh, F. E.; Holmes, M. A.; Zhao, J.; Chang, L.; Kawula, S.; Roehling, J. D.; Moulé, A. J. *J. Phys. Chem. C* **2014**, *118*, 14723−14731.
(49) Street, R. A.; Davies, D.; Khlyabich, P. P.; Burkhart, B.; Thompson, B. C. *J. Am. Chem. Soc.* **2013**, *135*, 986−989.
(50) Tuladhar, S. M.; Poplavskyy, D.; Choulis, S. A.; Durrant, J. R.; Bradley, D. D. C.; Nelson, J. *Adv. Funct. Mater.* **2005**, *15*, 1171−1182.
(51) Tvingstedt, K.; Vandewal, K.; Gadisa, A.; Zhang, F.; Manca, J.; Inganäs, O. *J. Am. Chem. Soc.* **2009**, *131*, 11819−11824.
(52) Dimitrov, S. D.; Bakulin, A. A.; Nielsen, C. B.; Schroeder, B. C.; Du, J.; Bronstein, H.; McCulloch, I.; Friend, R. H.; Durrant, J. R. *J. Am. Chem. Soc.* **2012**, *134*, 18189−18192.
(53) Behrends, J.; Sperlich, A.; Schnegg, A.; Biskup, T.; Teutloff, C.; Lips, K.; Dyakonov, V.; Bittl, R. *Phys. Rev. B: Condens. Matter Mater. Phys.* **2012**, *85*, 125206.
(54) Vandewal, B. K.; Gadisa, A.; Oosterbaan, W. D.; Bertho, S.; Banishoeib, F.; Van Severen, I.; Lutsen, L.; Cleij, T. J.; Vanderzande, D.; Manca, J. V. *Adv. Funct. Mater.* **2008**, *18*, 2064−2070.
(55) Panda, P.; Veldman, D.; Sweelssen, J.; Bastiaansen, J. J. A. M.; Langeveld-Voss, B. M. W.; Meskers, S. C. J. *J. Phys. Chem. B* **2007**, *111*, 5076−5081.
(56) Imoto, M.; Ikeda, H.; Fujii, T.; Taniguchi, H.; Tamaki, A.; Takeda, M.; Mizuno, K. *Org. Lett.* **2010**, *12*, 1940−1943.
(57) Hallermann, M.; Haneder, S.; Da Como, E. *Appl. Phys. Lett.* **2008**, *93*, 53307.
(58) Gromov, S. P.; Ushakov, E. N.; Vedernikov, A. I.; Lobova, N. A.; Alfimov, A. V.; Strelenko, Y. A.; Whitesell, J. K.; Fox, M. A. *Org. Lett.* **1999**, *1*, 1697−1699.
(59) Mulliken, R. S. *J. Am. Chem. Soc.* **1952**, *74*, 811−824.
(60) Paraschuk, D. Y.; Elizarov, S. G.; Khodarev, A. N.; Shchegolikhin, A. N.; Arnautov, S. A.; Nechvolodova, E. M. *JETP Lett.* **2005**, *81*, 467−470.
(61) Benson-Smith, J. J.; Goris, L.; Vandewal, K.; Haenen, K.; Manca, J. V.; Vanderzande, D.; Bradley, D. D. C.; Nelson, J. *Adv. Funct. Mater.* **2007**, *17*, 451−457.
(62) Heilig, M.; Domhan, M.; Port, H. *J. Lumin.* **2004**, *110*, 290−295.
(63) Zhang, D.; Horneber, A.; Mihaljevic, J.; Heinemeyer, U.; Braun, K.; Schreiber, F.; Scholz, R.; Meixner, A. J. *J. Lumin.* **2011**, *131*, 502−505.
(64) Tvingstedt, K.; Vandewal, K.; Zhang, F.; Inganäs, O. *J. Phys. Chem. C* **2010**, *114*, 21824−21832.
(65) Hallermann, M.; Da Como, E.; Feldmann, J.; Izquierdo, M.; Filippone, S.; Martín, N.; Jüchter, S.; von Hauff, E. *Appl. Phys. Lett.* **2010**, *97*, 23301.
(66) Clark, J.; Archer, R.; Redding, T.; Foden, C.; Tant, J.; Geerts, Y.; Friend, R. H.; Silva, C. *J. Appl. Phys.* **2008**, *103*, 124510.
(67) Anger, F.; Ossó, J. O.; Heinemeyer, U.; Broch, K.; Scholz, R.; Gerlach, A.; Schreiber, F. *J. Chem. Phys.* **2012**, *136*, 54701.
(68) Jarzab, D.; Cordella, F.; Gao, J.; Scharber, M.; Egelhaaf, H.-J.; Loi, M. A. *Adv. Energy Mater.* **2011**, *1*, 604−609.
(69) Arndt, A. P.; Gerhard, M.; Quintilla, A.; Howard, J. A.; Koch, M.; Lemmer, U. *J. Phys. Chem. C* **2015**, *119*, 13516−13523.

DOI: 10.1021/jacs.7b01622
J. Am. Chem. Soc. 2017, 139, 8474−8486

(70) Deotare, P. B.; Chang, W.; Hontz, E.; Congreve, D. N.; Shi, L.; Reusswig, P. D.; Modtland, B.; Bahlke, M. E.; Lee, C. K.; Willard, A. P.; et al. *Nat. Mater.* **2015**, *14*, 1130−1134.
(71) Broch, K.; Heinemeyer, U.; Hinderhofer, A.; Anger, F.; Scholz, R.; Gerlach, A.; Schreiber, F. *Phys. Rev. B: Condens. Matter Mater. Phys.* **2011**, *83*, 245307.
(72) Opitz, A.; Ecker, B.; Wagner, J.; Hinderhofer, A.; Schreiber, F.; Manara, J.; Pflaum, J.; Brütting, W. *Org. Electron.* **2009**, *10*, 1259−1267.
(73) Vandewal, K.; Tvingstedt, K.; Gadisa, A.; Inganäs, O.; Manca, J. V. *Phys. Rev. B: Condens. Matter Mater. Phys.* **2010**, *81*, 125204.
(74) Rau, U. *Phys. Rev. B: Condens. Matter Mater. Phys.* **2007**, *76*, 085303.
(75) Brigeman, A. N.; Fusella, M. A.; Yan, Y.; Purdum, G. E.; Loo, Y.-L.; Rand, B. R.; Giebink, N. C. *Adv. Energy Mater.* **2016**, *6*, 1601001.
(76) Ndjawa, G. O. N.; Graham, K. R.; Mollinger, S.; Wu, D. M.; Hanifi, D.; Prasanna, R.; Rose, B. D.; Dey, S.; Yu, L.; Brédas, J.-L.; McGehee, M. D.; Salleo, A.; Amassian, A. *Adv. Energy Mater.* **2017**, 1601995.
(77) Wilke, A.; Endres, J.; Hörmann, U.; Niederhausen, J.; Schlesinger, R.; Frisch, J.; Amsalem, P.; Wagner, J.; Gruber, M.; Opitz, A.; Vollmer, A.; Brütting, W.; Kahn, A.; Koch, N. *Appl. Phys. Lett.* **2012**, *101*, 233301.
(78) Karl, N. *Synth. Met.* **2003**, *133*−*134*, 649−657.
(79) Cheng, X.; Caironi, M.; Noh, Y.-Y.; Newman, C.; Wang, J.; Lee, M. J.; Banger, K.; Di Pietro, R.; Facchetti, A.; Sirringhaus, H. *Org. Electron.* **2012**, *13*, 320−328.
(80) Salzmann, I.; Heimel, G. J. *J. Electron Spectrosc. Relat. Phenom.* **2015**, *204*, 208−222.
(81) Opitz, A.; Wagner, J.; Brütting, W.; Hinderhofer, A.; Schreiber, F. *Phys. Status Solidi A* **2009**, *206*, 2683−2694.
(82) Pope, M.; Swenberg, C. E. *Electronic Processes in Organic Crystals and Polymers*; Oxford University Press: New York, 1999.
(83) Vandewal, K. *Annu. Rev. Phys. Chem.* **2016**, *67*, 113−133.
(84) Vandewal, K.; Tvingstedt, K.; Gadisa, A.; Inganäs, O.; Manca, J. V. *Nat. Mater.* **2009**, *8*, 904−909.
(85) Vandewal, K.; Goris, L.; Haeldermans, I.; Nesládek, M.; Haenen, K.; Wagner, P.; Manca, J. V. *Thin Solid Films* **2008**, *516*, 7135−7138.
(86) Hill, I. G.; Kahn, A.; Soos, Z. G.; Pascal, R. A., Jr. *Chem. Phys. Lett.* **2000**, *327*, 181−188.
(87) Hennessy, M. H.; Soos, Z. G.; Pascal, R. A., Jr.; Girlando, A. *Chem. Phys.* **1999**, *245*, 199−212.
(88) Xu, X.; Xiao, T.; Gu, X.; Yang, X.; Kershaw, S. V.; Zhao, N.; Xu, J.; Miao, Q. *ACS Appl. Mater. Interfaces* **2015**, *7*, 28019−28026.
(89) Méndez, H.; Heimel, G.; Opitz, A.; Sauer, K.; Barkowski, P.; Oehzelt, M.; Soeda, J.; Okamoto, T.; Takeya, J.; Arlin, J.-B.; et al. *Angew. Chem., Int. Ed.* **2013**, *52*, 7751−7755.

DOI: 10.1021/jacs.7b01622
J. Am. Chem. Soc. 2017, 139, 8474−8486